

PAPER • OPEN ACCESS

Normal zone propagation in various REBCO tape architectures

To cite this article: Christian Lacroix *et al* 2022 *Supercond. Sci. Technol.* **35** 055009

View the [article online](#) for updates and enhancements.

You may also like

- [Concept of a current flow diverter for accelerating the normal zone propagation velocity in 2G HTS coated conductors](#)
Christian Lacroix and Frederic Sirois
- [Analysis of the influence of the normal zone propagation velocity on the design of resistive fault current limiters](#)
Daniele Colangelo and Bertrand Dutoit
- [Thermal stability of quasi-isotropic strands with different cross-sections and with/without metal sheaths](#)
Guangyi Zhang, Yinshun Wang, Wei Liu *et al.*



IOP | ebooks™

Bringing together innovative digital publishing with leading authors from the global scientific community.

Start exploring the collection—download the first chapter of every title for free.

Normal zone propagation in various REBCO tape architectures

Christian Lacroix^{1,*} , Jaël Giguère¹, Simon-Mathieu Bergeron Hartman¹, Haïfa Ben Saad¹, Anthony Martin¹, Thomas Leduc¹, Maxime Gendron-Paul¹, Zakaria Bellil¹, Jean-Hughes Fournier-Lupien¹ , Lucile Moret¹, Pedro Barusco², Xavier Granados², Xavier Obradors² , Marcela Pekarčíková³, Fedor Gömöry⁴ , Veit Grosse⁵, Markus Bauer⁵ and Frédéric Sirois^{1,*} 

¹ Polytechnique Montréal, Montréal, QC H3C 3A7, Canada

² Institut de Ciència de Materials de Barcelona, Barcelona, Spain

³ Faculty of Materials Science and Technology in Trnava, Slovak University of Technology in Bratislava, Trnava, Slovakia

⁴ Institute of Electrical Engineering, Slovak Academy of Sciences, Bratislava, Slovakia

⁵ THEVA Dünnschichttechnik GmbH, Ismaning, Germany

E-mail: christian.lacroix@polymtl.ca and f.sirois@polymtl.ca

Received 3 November 2021, revised 17 February 2022

Accepted for publication 21 February 2022

Published 30 March 2022



CrossMark

Abstract

The normal zone propagation velocity (NZPV) of three families of REBCO tape architectures designed for superconducting fault current limiters and to be used in high voltage direct current transmission systems has been measured experimentally in liquid nitrogen at atmospheric pressure. The measured NZPVs span more than three orders of magnitude depending on the tape architectures. Numerical simulations based on finite elements allow us to reproduce the experiments well. The dynamic current transfer length (CTL) extracted from the numerical simulations was found to be the dominating characteristic length determining the NZPV instead of the thermal diffusion length. We therefore propose a simple analytical model, whose key parameters are the dynamic CTL, the heat capacity and the resistive losses in the metallic layers, to calculate the NZPV.

Keywords: REBCO tape, normal zone propagation velocity, quench

(Some figures may appear in colour only in the online journal)

1. Introduction

High-temperature superconductor tapes based on REBCO, where RE stands for rare-earth, are promising candidates for enabling breakthrough technologies such as nuclear fusion [1], protontherapy [2] and high efficiency superconducting machines [3]. Among the promising applications, resistive superconducting fault current limiters (SFCLs) are an interesting solution to ensure safety and resilience in power grids. In the FASTGRID project [4], several REBCO tape architectures were investigated in order to significantly

increase the electric field that can be supported by a REBCO tape during a fault current event occurring in a high voltage direct current electrical network. Increasing the electric field allows us to limit the length of the REBCO tape required, thus reducing the footprint and cost of the SFCL [5]. In particular, it was shown that soldering a 500 μm thick Hastelloy shunt on a REBCO tape ($I_c > 800 \text{ A cm}^{-1}$ width at 77 K, self-field) allowed the tape to sustain an electric field over 100 V m^{-1} for 50 ms [6].

One of the main issues regarding REBCO tapes is the low normal zone propagation velocity (NZPV), which, over the years, has been investigated using different experimental techniques [7–14]. In coil and magnet applications, this makes quench detection very difficult and implies the development of

* Authors to whom any correspondence should be addressed.



innovative solutions to avoid burning the coil [15]. In SFCL, the low NZPV of REBCO tapes coupled to inhomogeneities of their local critical current make them prone to local degradation in the case of a prospective fault current close to their average critical current [16].

Therefore, understanding the parameters that affect the NZPV becomes essential when designing tape architectures to be used in specific applications. For example, it has been demonstrated experimentally that the addition of a metallic shunt such as copper or stainless steel reduces the NZPV [17, 18]. In this work, the NZPV of REBCO tapes with different architectures fabricated in the context of the FASTGRID project was investigated both experimentally and numerically at 77 K. The results were analyzed to highlight the main parameters affecting the NZPV. This allowed us to propose an analytical expression for the calculation of the NZPV.

2. Samples investigated

In this section, we describe all the architectures investigated in this work. A cross-section view of each architecture is shown in figure 1.

2.1. Bare REBCO tapes

The base REBCO tapes used in this work were 12 mm wide REBCO tapes produced by THEVA Dünnschichttechnik GmbH [19–21]. Explicitly, inclined substrate deposition was first used to deposit 3.5 μm thick MgO buffer layers on a 97 μm thick untextured Hastelloy substrate. A 3.1 μm thick GdBaCuO layer was subsequently deposited at 700 °C on the MgO buffer layers. This tape architecture constitutes what we call the ‘base THEVA tape’ later in this section. Afterwards, a Ag layer having a thickness between 1 and 2 μm was thermally evaporated all around the base THEVA tape. Two samples based on this architecture were characterized: a tape with a total of 2 μm of Ag (1 μm on the REBCO side and 1 μm on the substrate side), called ‘Ag2’ later on, and a tape with a total of 4 μm of Ag (2 μm on the REBCO side and 2 μm on the substrate side), called ‘Ag4’.

2.2. REBCO tape with a CuNi shunt

A 100 μm thick and 12 mm wide Cu60Ni40 shunt was soldered with a SnAg3.0Cu0.5 alloy on the REBCO side of a base THEVA tape with a 1 μm thick surrounding Ag layer. The thickness of the solder varied locally from 5 to 10 μm according to scanning electron microscopy. This sample is called ‘CuNi100’ later on.

2.3. REBCO tape with a Hastelloy shunt

A 500 μm thick and 12 mm wide Hastelloy shunt with a nominal 10 μm thick surrounding tin layer was soldered on a base THEVA tape with a 1.6 μm thick surrounding Ag layer. The shunt was soldered on the REBCO side of the tape. A custom soldering process was developed especially for this purpose by THEVA. This sample is called ‘Hast500’ later on.

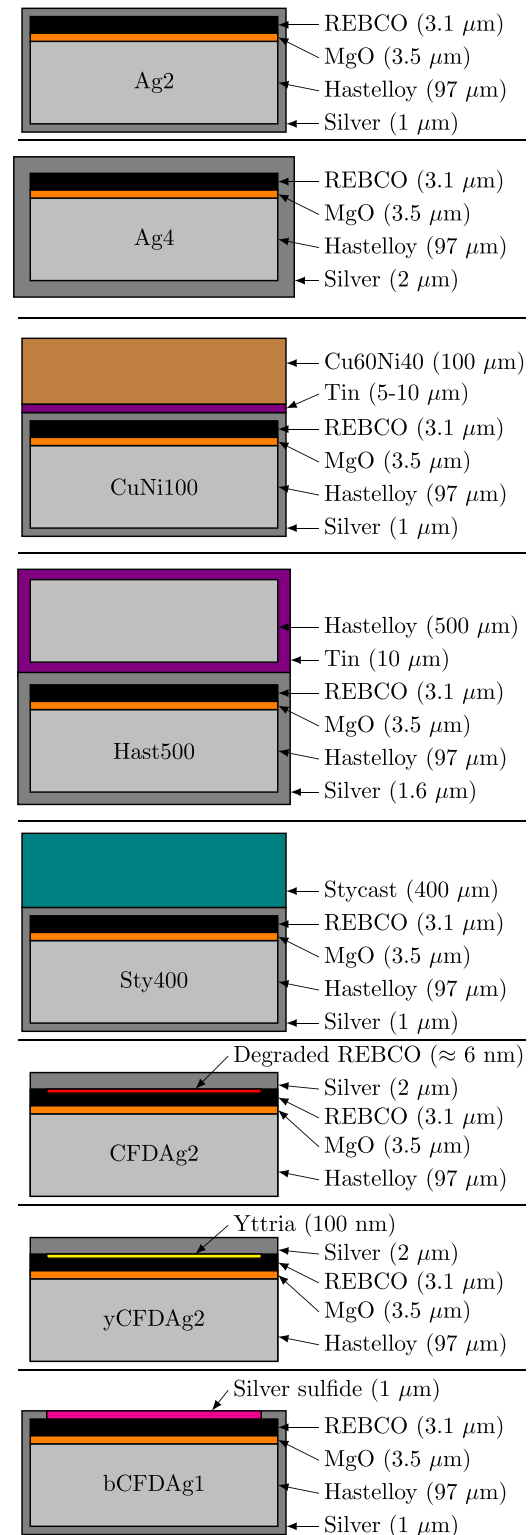


Figure 1. Cross-section view of the different tape architectures investigated in this work (not to scale). See text for a detailed description of each type of architecture. Note that, for all architectures except CFDAg2 and yCFDAg2, the silver layer is surrounding the base THEVA tape.

2.4. REBCO tape covered with Stycast

A base THEVA tape with a 1 μm thick surrounding Ag layer was covered with a 400 μm -thick epoxy coating on the

REBCO side. The epoxy consisted of Stycast 2850 FT (Catalyst 11) mixed with SiC filler (20 vol.% of SiC). Furthermore, E-glass fibers with a diameter of 14 μm were added in the coating to improve the mechanical properties. Further details on the fabrication process can be found in [22]. This sample is called ‘Sty400’ later on.

2.5. CFD tapes

The current flow diverter (CFD) concept was introduced in [23]. Two different fabrication routes were used to fabricate CFD tapes. The first route corresponds to that described in [24]. In this route, base THEVA tapes with a 1 μm thick surrounding Ag layer were used. First, the silver on the Hastelloy substrate and on the sides of the tape was completely removed using chemical etching. On the REBCO side, a shadow mask was used to remove the silver solely on the central part of the tape. The silver strip that was etched had a width of 10.8 mm. After the chemical etching, the only silver left was two 0.6 mm wide strips located on the two edges of the REBCO side of the tape. Finally, a 2 μm thick silver layer was deposited on the REBCO side using DC sputtering. This sample is called ‘CFDAg2’ later on.

The second route is described in details in [25]. In this second route, chemical solution deposition with propionate yttrium solution precursors was used to create a yttria layer covering 85%–90% of the REBCO layer on a base THEVA tape. To form the CFD pattern, before executing the deposition, a polyimide mask was used to protect the remaining surface ($\approx 10\%$) along the edges of the REBCO layer where no yttria layer was required. Spin coating of the yttrium propionate solution was used to obtain ultimately a yttria (Y_2O_3) layer having a thickness of ≈ 100 nm. The pyrolysis of the yttrium propionate solution to form the yttria was performed in a tubular furnace heated at temperatures ranging from 350 $^\circ\text{C}$ to 450 $^\circ\text{C}$ in 1 bar of oxygen atmosphere for 1 h. Afterwards, a 2 μm thick silver layer was deposited on the REBCO side using DC sputtering. Finally, the tape was re-oxygenated at 400 $^\circ\text{C}$ to reduce the interfacial resistance Ag/REBCO solely on the yttria-free edges of the REBCO. This sample is called ‘yCFDAg2’ later on.

2.6. bCFD tape

The buffer layers-CFD (or bCFD) architecture was proposed in [26] and experimentally demonstrated in [18, 27]. In this work, tapes with a bCFD architecture were fabricated using a sulfidation process. Sulfidation is the chemical reaction of a solid material, such as a metal/alloy, with a sulfur containing environment. This reaction leads to the formation of a sulfur-based compounds and it is known to form silver sulfide (Ag_2S) on the surface of silver. Ag_2S is a semiconductor compound whose resistivity is several orders of magnitude higher than silver. This process was used on a base THEVA tape with a 1 μm thick surrounding Ag layer to change the Ag thickness ratio between the upper and bottom layer of the silver shunt and achieve the bCFD effect. Prior to the sulfidation, the tape was partially covered with polyimide tape along the edges

Table 1. Measured critical currents at 77 K (I_{c0}) using the criterion $E_c = 100 \mu\text{V m}^{-1}$ and power law indexes (n -value) in self-field prior to NZPV measurements. The dynamic CTL (λ_d) for $I_{op} = I_{c0}$ during quench, as obtained from numerical calculations, is also given.

Sample	I_{c0} (A)	n -value	λ_d (mm) for $I_{op} = I_{c0}$
Ag2	567	38.0	2.7
Ag4	828	28.4	2.2
CuNi100	639	32.7	1.0
Hast500	694	28.6	1.2
Sty400 ^a	650	—	2.8
CFDAg2	639	32.7	9.6
yCFDAg2	348	18.5	9.0
bCFDAg1	335	23.6	10.4

^a Critical current measured by THEVA using TapeSTAR.

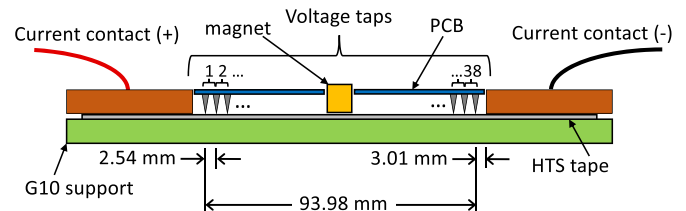


Figure 2. Illustration of the sample holder used to perform NZPV measurements.

leaving the central part of the tape on the REBCO side exposed with a width varying between 10 and 11 mm. The sulfidation, which lasted 3.5 h, was performed in a closed system with a vapor pressure of liquid sulfur at 130 $^\circ\text{C}$. After the sulfidation, the central shunt part uncovered with polyimide had a dark black color characteristic of Ag_2S with a mild increased roughness. This sample is called ‘bCFDAg1’ later on. More details of this bCFD-sulfide process will be given elsewhere.

3. Experimental details

The critical current (I_{c0}) and power law index (n -value) of all samples were measured at 77 K with a pulsed current method [6], except for sample Sty400, whose critical current was measured using TapeSTAR [19], and are given in table 1.

The NZPV of the tapes was measured using a homemade pulsed current source. Custom PCB-based sample holders were fabricated in order to measure simultaneously up to 38 differential voltages along 100 mm long REBCO tapes (see figure 2). The distance between the centres of two adjacent voltage taps is 2.54 mm. A cylindrical NdFeB magnet was used to locally reduce the critical current of the sample to induce the initial quench.

To perform NZPV measurements, the sample was first immersed in a liquid nitrogen bath at atmospheric pressure. Then, 5–30 ms long current pulses of constant amplitude (close to the critical current of each sample) were applied on the sample. The heat generated at the location of the NdFeB

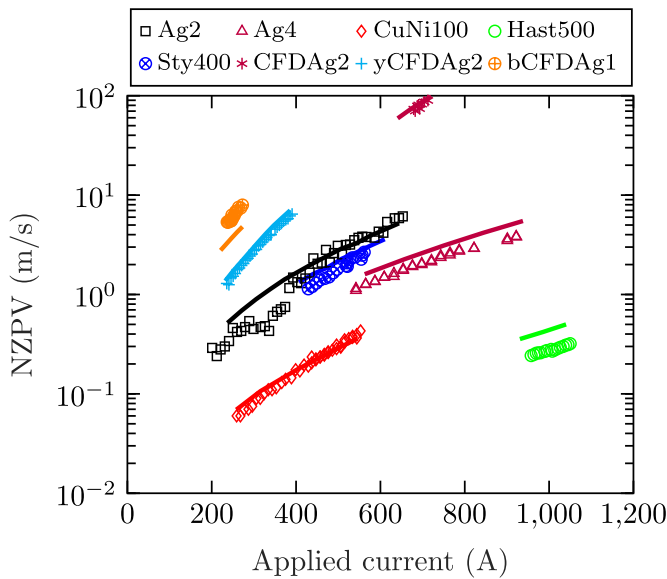


Figure 3. Experimental NZPV obtained at 77 K in self-field (symbols) versus applied current for all samples. The solid lines were calculated with the numerical model described in section 5.1.

magnet triggered a quench in the middle of the sample. During quench propagation, the time evolution of the voltage drop along the sample was recorded with a 80-channels data acquisition card from National Instruments. The NZPV was calculated by taking the time delay between two adjacent differential signals to reach a given voltage level, divided by the distance between the taps, that is 2.54 mm. This measurement has been repeated for different current pulse amplitudes to obtain the dependance of the NZPV with the applied current. For more examples about NZPV measurements, see [18, 24, 28].

4. NZPV measurements

In figure 3, the experimental NZPV values obtained versus the operating current I_{op} (or applied current) are presented. We first note that the NZPV of sample Ag2 is relatively high with respect to the NZPV values reported for REBCO tapes in the literature, reaching up to 6 m s^{-1} at 650 A. This is because its critical current is approximately three times larger than most REBCO tapes whose NZPV is reported in the literature, since the thickness of the REBCO layer in THEVA tapes is $3.1 \mu\text{m}$ (rather than $1 \mu\text{m}$). Furthermore, REBCO tapes are often covered with a surrounding $20 \mu\text{m}$ thick copper layer, which strongly reduces the NZPV. In figure 3, we can see the effect of a thicker stabilizing layer by comparing the NZPV values of sample Ag2 with the NZPV of sample Ag4, whose NZPV is approximately three times lower than sample Ag2.

We observe that the NZPV is strongly reduced when a thick metallic shunt is added. This is explained by two reasons. Firstly, the thermal mass of the tape is much larger, which means that more energy is required to increase its temperature. Secondly, the shunt and the tin used to solder the shunt are conductive, which reduces Joule heating. In particular, in the case of sample Hast500, the NZPV becomes very low

($\approx 0.27 \text{ m s}^{-1}$ at 1000 A). In the case of sample CuNi100, the reduction in NZPV is less drastic. For example, at 500 A, the NZPV is approximately one order of magnitude lower than that of sample Ag2.

If we compare the NZPV of sample Sty400 with that of sample Ag2, we observe that the addition of a Stycast shunt induces only a slight reduction ($\approx 25\%$) of the NZPV. Since Stycast is an electrical insulator, it does not affect the resistance per unit length of the tape and thus Joule heating. However, Stycast increases the total thermal mass of the sample. As a consequence, a larger amount of energy is required to increase the temperature of the tape, which reduces the NZPV.

In the case of samples CFDAg2 and yCFDAg2, the NZPV is approximately 6–8 times higher than that of sample Ag2. This is consistent with previous results reported in the literature for CFD tapes [24, 26]. In the case of sample bCFDAg1, the NZPV is very high, almost 17 times higher than that of sample Ag2. The fact that the total silver thickness is $1 \mu\text{m}$ instead of $2 \mu\text{m}$ makes the comparison more difficult but it is clear that the reduction of the silver layer thickness from 2 to $1 \mu\text{m}$ cannot induce a 17-fold increase in the NZPV. This huge increase in NZPV is a consequence of the bCFD architecture.

5. Comparison with numerical simulations

5.1. Description of the numerical model

The model used to perform the simulations is a modified version of the 3D model described in [6]. It has been implemented in the COMSOL Multiphysics 5.5 software package and uses two modules, namely the Electric Currents and Heat Transfer in Solids modules.

In the model, we compute the electrical potential V and temperature T using the current continuity and the heat transfer equations, respectively. These equations are coupled through the electric losses and are solved with the built-in time transient solver. A current $I(t)$ is imposed at one end of the tape while the other end is grounded. At both ends of the tape, we consider that the temperature gradient is zero, i.e. $\mathbf{n} \cdot \nabla T = 0$, where \mathbf{n} is a unitary vector perpendicular to the surface. For the remaining boundaries, we used $\mathbf{n} \cdot (k \nabla T) = h(T - T_0)$, which represents the cooling power of liquid nitrogen, where h is a heat transfer coefficient representing the thermal exchange between the tape surfaces and the surrounding liquid nitrogen [29]. It is worth noting that the effect of this thermal exchange on the results presented below is small and does not affect the main conclusions of this work. It has only been mentioned here for the sake of completeness.

To minimize the computation time of this 3D numerical model, the number of elements is reduced by taking advantage of the symmetries of the problem. To further reduce the computation time, the buffer layers and the resistive interface between the superconducting layer and the silver were approximated as 2D domains, i.e., as if they were infinitely thin (see [23] for further details).

The sample geometry used was that of the REBCO tape architectures described in section 2. Regarding the material properties, most of them could be found in the literature or

were directly accessible within COMSOL Multiphysics 5.5. The only exceptions were the electrical conductivity of silver and GdBCO. The electrical conductivity of silver was determined from resistance measurements, as explained in [6]. The electrical conductivity of GdBCO was approximated using a power-law model in the flux creep and flux flow regimes (σ_{sc}), while the transition from the superconducting state to the normal state (σ_n) was modeled by assuming two resistances in parallel, i.e.

$$\sigma_{GdBCO}(T) = \sigma_{sc}(T) + \sigma_n(T), \quad (1)$$

where

$$\sigma_{sc}(T) = \frac{J_c(T)}{E_0} \left(\frac{\|E\|}{E_0} \right)^{\frac{1-n(T)}{n(T)}} \quad (2)$$

is the electrical conductivity in the superconducting state, $\sigma_n(T)$ is the electrical conductivity in the normal state, $J_c(T)$ is the critical current density, $\|E\|$ is the norm of the electric field, E_0 is the electric field criterion (10^{-4} V m^{-1}) and $n(T)$ is the power law index. The temperature dependencies of $J_c(T)$ and $n(T)$ for each sample were determined using the values given in table 1 and the method described in [6].

Finally, to emulate the reduction of the local critical current due to the magnetic field created by the cylindrical NdFeB magnet, a low J_c region was included in the simulated REBCO tape.

5.2. Simulated vs experimental NZPV values

The NZPV obtained from numerical simulations are presented in figure 3 (solid lines). We observe that, globally, the numerical model reproduces quite well the experimental data. Discrepancies are mainly observed on tapes either with very low or very high NZPV values.

In the case of sample Hast500, we observe that, the calculated values are higher than the experimental values. This could be explained as follows. Since sample Hast500 has a very low NZPV, the normal zone spreads only over a few mm during a quench experiment, which makes it difficult to determine a precise value of the experimental NZPV. Furthermore, it is possible that the tape properties vary strongly along the sample length. Indeed, scanning electron microscopy analysis (not shown) revealed that the thickness of the tin layer between the silver layer and the Hastelloy shunt can vary strongly along the length of the tape (from 2 up to 18 μm) in these samples. It is thus possible that the thickness of the tin layer at the magnetic defect location was in reality larger than the value used in the simulation (12 μm). As discussed before, a thicker metallic layer translates into a lower NZPV.

In the case of sample bCFDAg1, we observe that the simulated NZPV is lower than the experimental value. One possible explanation for this is the limited length of the samples used in the experiments ($\approx 100 \text{ mm}$). This, coupled with the fact that the NZPV is very high, causes the whole sample to quench almost instantaneously once a hot spot is generated, which makes harder the extraction of the NZPV from the experimental data.

5.3. Shape of the normal zone

In figure 4, 2D maps of the temperature in the REBCO layer during a normal zone propagation are presented for an operating current (I_{op}) equal to the critical current at 77 K (I_{c0}). The temperature scale was reduced between 80 and 100 K in order to help see the details at the boundary of the normal/superconducting regions (N/SC). Note that the normal zone spreads from right to left.

Firstly, we observe that sample Ag2 has a parabolic N/SC boundary. This is due to the current crowding at the edges of the tape, similar to the ‘bCFD’ effect, which generates heat at the edges of the tape. In comparison, the curvature is less pronounced in the case of sample Ag4, and even less pronounced in the case of samples CuNi100 and Hast500, where it becomes almost a straight line. This is because the amount of metal on the REBCO side is increased, which reduces the amount of current flowing into the silver layer on the substrate side, and also the current density at the edges of the tape.

In the case of sample Sty400, the curvature is very similar to that of sample Ag2. This is not surprising since sample Sty400 has the same architecture as sample Ag2, except for the insulating shunt made of Stycast on the REBCO side. Thus, the amount of current flowing in the silver on the substrate side is the same as in sample Ag2.

In the case of samples CFDAg2, yCFDAg2 and bCFDAg1, we observe that the curvature of the N/SC boundary is very pronounced. For these samples, the current density at the edges of the tape is increased due to the CFD architecture. Also, we note that the N/SC boundary is blurred, indicating that the temperature gradient is smaller than in tapes with no CFD architecture.

5.4. Dynamic CTL

When a current is injected in a REBCO tape, it must transfer from the metallic layers surrounding the tape to the superconducting layer. The distance required for this transfer to occur is called the current transfer length (CTL). In the literature [30], the CTL (λ_s) is defined by

$$I_{shunt}(x) = I_{op} \exp(-x/\lambda_s), \quad (3)$$

where I_{shunt} is the current flowing in the metallic layers at the distance x from the current injection location. According to equation (3), λ_s corresponds to the distance x where $I_{shunt}(\lambda_s)/I_{op} = e^{-1} \approx 0.37$.

It has been demonstrated in previous works that the NZPV is proportional either to the CTL or the thermal diffusion length (λ_t), depending on the electrical resistance at the interface between the REBCO layer and the silver [31]. The thermal diffusion length is derived from the heat equation (see equation (5) in section 5.6) and is given by $\lambda_t = \sqrt{D_T \Delta t}$, where $D_T = k/(\rho_m C_p)$ is the thermal diffusivity,

$$\Delta t = \frac{wh_{tot} \langle \rho_m C_p \rangle \Delta T}{I_{op}^2 R_{90K}} \quad (4)$$

is the time required for the tape to reach the transition temperature T_t , $\Delta T = T_t - T_{op}$, T_{op} is the operating temperature,

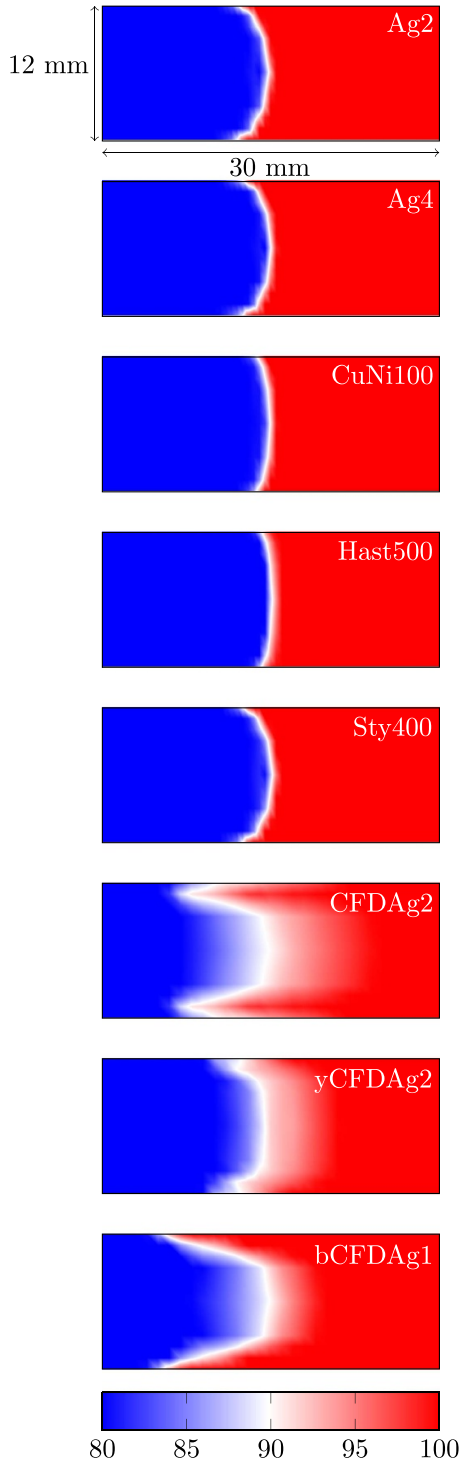


Figure 4. Two-dimensional maps obtained from numerical simulations of the temperature in the REBCO layer during a normal zone propagation at 77 K and $I_{op} = I_{c0}$. The normal zone (red) spreads from right to left. The units of the colorbar are Kelvins.

R_{90K} is the tape resistance in the normal state at 90 K ($\Omega \text{ m}^{-1}$), w is the width of the tape (m) and h_{top} is the total thickness of the tape (m). In the literature, T_t is defined as the temperature at which the electric losses in the REBCO layer are equal to the electric losses in the metallic layers, for a given transport current. In the case of LTS, the following approximation is

often made, that is $T_t \approx (T_c + T_{cs})/2$, where T_{cs} is the current sharing temperature, which corresponds to the temperature at which the critical current value is equal to the applied current, i.e. $I_{op} = I_c(T_{cs})$. Assuming that I_c varies linearly with the temperature, we obtain $T_{cs} = T_c - (T_c - T_{op})(I_{op}/I_{c0})$, where I_{c0} is the critical current at T_{op} . The quantity $\langle \rho_m C_p \rangle$ ($\text{J}(\text{K}\cdot\text{m}^3)^{-1}$) corresponds to an average value of the volume heat capacity at $T = T_t$, weighted by the thickness of each layer [15].

For the architectures considered in this work, since the thickness of the metallic shunt is either small or has a low thermal conductivity, this translates into a low λ_t value. A rough estimation gives $\lambda_t \approx 100 \sim \mu\text{m}$ or less. As will be shown later, the CTL of the samples investigated in this work is a least one order of magnitude higher than λ_t , which means the CTL is the characteristic length that ‘drives’ the NZPV.

In [32], the concept of ‘dynamic CTL’ (λ_d) has been introduced and defined as the CTL during the propagation of a quench. It has been shown that λ_d can be different from the classic definition of the CTL, which we will call thereafter the ‘static CTL’ (λ_s). The main difference between λ_d and λ_s originates from the thermal dynamics of the normal zone propagation. In other words, the origin of λ_s is purely electric while the origin of λ_d is a mix of thermal and electrical phenomena.

In a 2D architecture such as substrate/buffer layers/REBCO/silver, we have $\lambda_d = \lambda_s$ because the heat generation is invariant along the width of the tape. However, most commercial architectures are rather 3D architectures since silver covers all sides of the tape. As a consequence, upon a local quench, current crowding occurs at the edges of the tape because a significant fraction of the current must flow around the buffer layers to reach the silver on the substrate side [26]. This triggers inhomogeneous heating along the width of the tape (the N/SC boundary has a ‘U-shape’ as seen in figure 4) that increases the CTL and thus, the NZPV. This phenomenon is also known as the ‘bCFD’ effect [27]. In the case of a 2D architecture, the N/SC boundary is a straight line.

As discussed previously, according to equation (3), the CTL corresponds to the distance where the current flowing in the metallic layers is 37% of the operating current, or inversely, the distance where the current flowing in the superconducting layer is 63% of the operating current. The dynamic CTL was determined from numerical simulations by looking at the total current flowing in the REBCO layer along the length of the tape, as shown in figure 5. The value of λ_d corresponds to the distance required for 63% of the current to transfer from the stabilizer to the REBCO layer.

The dynamic CTL was determined for all samples with an operating current equal to their respective critical current at 77 K ($I_{op} = I_{c0}$). The results are given in table 1. We note that $\lambda_d \geq 1$ mm for all samples. Therefore, as mentioned earlier, since λ_d is at least one order of magnitude higher than λ_t ($\approx 100 \mu\text{m}$), λ_d is the dominant characteristic length and thus dictates the amplitude of the NZPV.

In table 1, we observe that λ_d is the highest in the case of samples CFDAg2, yCFDAg2 and bCFDAg1. This is not surprising since these architectures were specifically designed to enhance λ_d [23, 26]. Indeed, when looking at

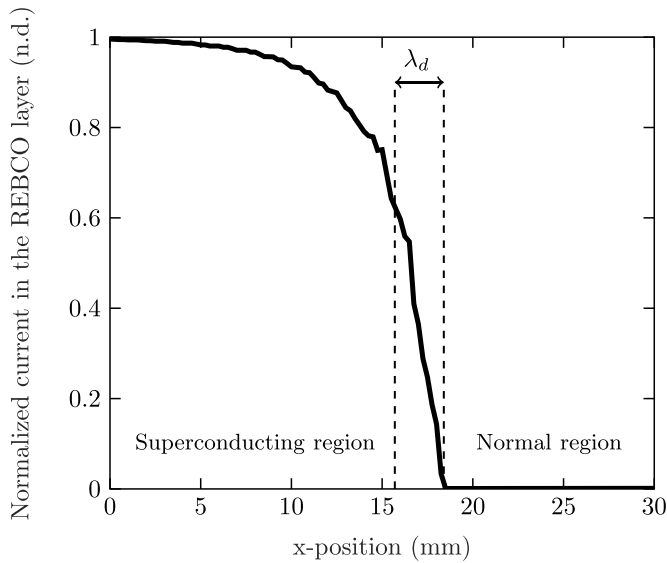


Figure 5. Total current in the REBCO layer during a normal zone propagation in the case of sample Ag2. The dynamic CTL (λ_d) corresponds to the distance between the x -position where the current in the REBCO layer becomes zero and the location where the current corresponds to 63% of the applied current. Here, we have $\lambda_d = 2.7$ mm.

the 2D temperature maps (figure 4), we clearly see the typical ‘U-shape’ associated with the CFD and bCFD architectures [27].

In the case of samples Ag2, Ag4 and Sty400, the λ_d values range between 2.3 and 2.8 mm. This is 2–3 times higher than tapes with a thick metallic shunt (CuNi100 and Hast500). This higher λ_d is due to the presence of the bCFD effect, but to a much lesser extent than in samples CFDAg2, yCFDAg2 and bCFDAg1. In the case of samples CuNi100 and Hast500, most of the current flows into the metallic layers located on the REBCO side, so λ_d is rather small (almost no bCFD effect is present).

5.5. Effect of the heat dissipation in the shunt

Our numerical calculations indicate that λ_d is the same with or without an insulating shunt (see λ_d of samples Ag2 and Sty400 in table 1). However, as observed in figure 3, there is a slight reduction of the NZPV of sample Sty400 in comparison with sample Ag2. This can be attributed to the absorption of heat by the insulating shunt [22]. Indeed, in figure 6, the time evolution of temperature at the defect location obtained from numerical simulations is compared in the case of samples Ag2, Sty400 and CuNi100. We observe that the temperature at the defect location in sample Sty400 is reduced in comparison to sample Ag2, thanks to the heat absorption in the insulating shunt.

The difference between a metallic shunt and an insulating shunt is that the metallic shunt not only adds thermal mass, but also reduces Joule losses. As a consequence, this drastically reduces the temperature and the NZPV. This can be observed from the time evolution of the temperature at the defect location in figure 6 and also, from the NZPV in figure 3.

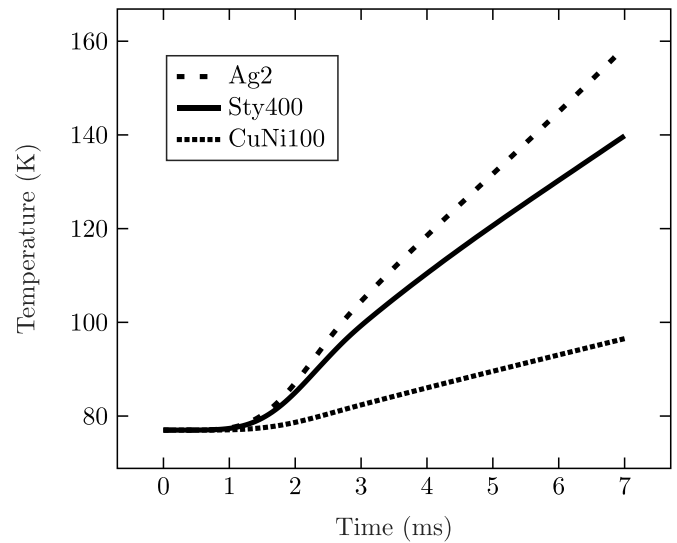


Figure 6. Comparison of the calculated temperature at the defect location over time for an applied current of 405 A in the case of samples Ag2, Sty400 and CuNi100. The rising time of the applied current is 3 ms, then the current remains constant.

5.6. Analytical model of NZPV

We have shown above that the NPZV in REBCO tapes can be predicted using FEM simulations. However, it would be useful to have a simple analytical model that could predict the NZPV accurately. An analytical model does not only allow performing rapid calculations but, it also helps to understand the underlying physics.

Analytical models to calculate the NZPV in superconducting wires have been proposed several decades ago for low-temperature superconductor wires [33, 34]. These models have been applied successfully on REBCO tapes with a thick copper stabilizing layer (total thickness of 40 μm) [35]. More recently, Bonura and Senatore proposed an improved formula to calculate the NZPV of REBCO tapes with 40 μm of copper [36].

One of the main assumptions of these models is that the dominant characteristic length of the quench behavior is the thermal diffusion length (λ_T). This is indeed the case when a thick metallic shunt is present in REBCO tapes. As discussed in section 5.4, for the tape architectures investigated in this work, the NZPV is rather dominated by λ_d instead of λ_T . Indeed, if we calculate the NZPV using the expressions used by Dresner [34], or Iwasa [35] in the case of sample Ag2, we obtain for both expressions $\approx 0.2 \text{ m s}^{-1}$ for an applied current of 540 A, which is 17 times lower than the actual measured value 3.5 m s^{-1} .

Here, we propose a simple analytical model to calculate the NZPV of REBCO tapes when λ_d is the dominant characteristic length. Since the quench of a superconducting tape is a heat-driven phenomena [33–35], it is justified to develop the model starting from the heat equation, which is written as follows:

$$\rho_m C_p (T) \frac{\partial T}{\partial t} + \nabla \cdot (-k(T) \nabla T) = Q_j, \quad (5)$$

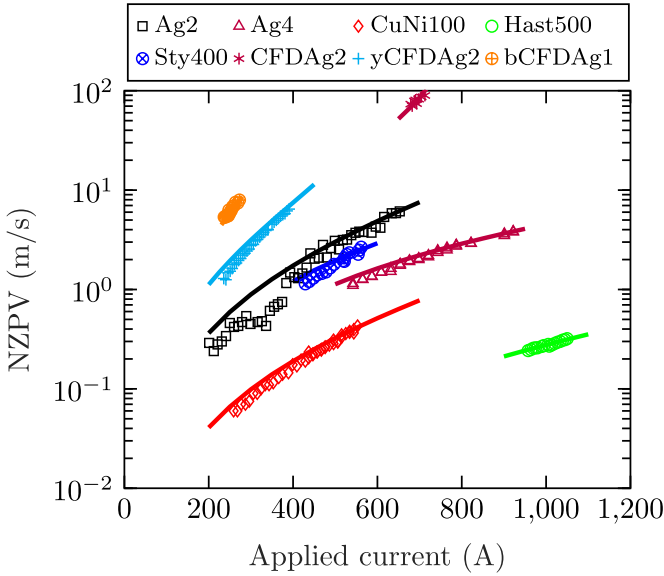


Figure 7. Experimental NZPV obtained at 77 K in self-field (symbols) versus applied current for all samples. The solid lines were calculated with equations (6) and (7).

where ρ_m is the mass density, $C_p(T)$ is the heat capacity, $k(T)$ is the thermal conductivity and $Q_j = \rho(T)J^2$ represent the electric losses in the tape.

If λ_d is the dominant characteristic length of the quench dynamics, it means that the volume expansion rate of the normal zone corresponds to the time required to heat the tape within a length λ_d in front of the normal zone/superconducting boundary. We suppose that λ_r has no impact on the NZPV, which allows to neglect the term $\nabla \cdot (-k(T)\nabla T)$ in equation (5) and leads to equation (4). The NZPV is thus given by

$$\text{NZPV} = \lambda_d / \Delta t, \quad (6)$$

and Δt by equation (4).

According to [36], the approximation $T_t \approx (T_c + T_{cs})/2$ remains a good estimation of T_t for REBCO when $T \geq 20$ K. Nevertheless, we propose to use a more general expression for T_t , that is $T_t \approx \alpha T_{cs} + (1 - \alpha)T_c$, where α can have any value between 0 and 1. We can then express ΔT as follows

$$\Delta T = (T_c - T_{op}) \left(1 - \frac{\alpha I_{op}}{I_{c0}} \right). \quad (7)$$

Equations (6) and (7) were used to fit the experimental values of NZPV for all samples. For the fitting, all the parameters were known except α and T_c . We note that λ_d must *a priori* be calculated numerically. Using a trial and error method, it was found that a value of $T_c = 95$ K yielded the best results for all samples. We note that this value is slightly higher than T_c values reported in the literature for REBCO, which are typically 92–94 K. Once T_c was fixed, the parameter α was adjusted to obtain the best results.

The results of the fit are shown in figure 7, while the values of α and T_t for $I_{op} = I_{c0}$ are given in table 2. We observe that

Table 2. Values of α used to calculate the solid lines in figure 7. The corresponding transition temperature T_t for $I_{op} = I_{c0}$ is also given.

Sample	α	T_t (K) for $I_{op} = I_{c0}$
Ag2	0.40	87.8
Ag4	0.05	94.1
CuNi100	0.45	86.9
Hast500	0.22	90.2
Sty400	0.19	90.9
CFDAg2	0.78	80.9
yCFDAg2	0.50	86.0
bCFDAg1	0.76	81.3

we can separate the samples into two groups, the ‘standard’ tapes and the ‘CFD’ tapes. In the standard case, we note that $\alpha < 0.5$, while in the CFD case, $\alpha \geq 0.5$. Translated in terms of the transition temperature T_t , it means that T_t is lower for CFD tapes than for standard tapes. This suggests that the energy required to induce a normal zone in CFD tapes is reduced. This is in agreement with preliminary measurements of the minimum quench energy (MQE) performed on CFD tapes [37], which seems to indicate that the MQE is lower in CFD tapes than in standard REBCO tapes.

6. Conclusion

The NZPV of three families of REBCO tape architectures has been investigated experimentally and numerically. It was shown that the experimental NZPV values can extend over more than three orders of magnitude, depending on the tape architecture and applied current. Also, it was demonstrated that the dynamic CTL (λ_d) was one of the key parameters to increase the NZPV. Furthermore, our results demonstrated that a higher heat capacity and a thicker metallic shunt reduces the NZPV. These discoveries led us to propose a simple analytical model to calculate the NZPV, in the case where the dominant characteristic length is λ_d rather than the thermal diffusion length λ_r .

For several years, the NZPV of REBCO tapes was considered as a parameter that cannot be modified (or just slightly). We have shown that it can vary over several orders of magnitude with the appropriate tape architecture. As a rule of thumb, we can assume that for a REBCO tape with a thick metallic shunt, its low electrical resistance, high heat capacity and small λ_d will lead to a low NZPV value. On the other hand, for a REBCO tape with a thin stabilizer, its high electrical resistance, low heat capacity and large λ_d (especially for a CFD architecture) will lead to a large NZPV value. Hopefully, these findings will guide tape manufacturers and engineers to design the best tape architecture for a specific application when quench dynamics is a key issue.

Data availability statement


All data that support the findings of this study are included within the article (and any supplementary files).

Acknowledgments

The authors acknowledge the funding of this research by FASTGRID Project (EU-H2020, 721019), the Projects COACHSUPENERGY (MAT2014-51778-C2-1-R), SUMATE (RTI2018-095853-BC21 and RTI2018-095853-B-C22) from the Spanish Ministry of Economy and Competitiveness which were cofunded by the European Regional Development Fund, the Project 2017-SGR 753 from Generalitat de Catalunya and the COST Action NANOCOBYBRI (CA16218). Polytechnique Montréal authors also acknowledge NSERC (Canada), FRQNT (Québec), the RQMP infrastructure and CMC microsystems for financial support. ICMAB authors also acknowledge the Center of Excellence awards Severo Ochoa SEV-2015-0496 and CEX2019-000917-S.

ORCID iDs

Christian Lacroix  <https://orcid.org/0000-0002-1648-1879>

Jean-Hughes Fournier-Lupien  <https://orcid.org/0000-0002-0792-2548>

Xavier Obradors  <https://orcid.org/0000-0003-4592-7718>

Fedor Gömöry  <https://orcid.org/0000-0002-2278-5123>

Frédéric Sirois  <https://orcid.org/0000-0003-0372-9449>

References

- [1] Bruzzone P, Fietz W H, Minervini J V, Novikov M, Yanagi N, Zhai Y and Zheng J 2018 *Nucl. Fusion* **58** 103001
- [2] Godeke A et al 2020 *Supercond. Sci. Technol.* **33** 064001
- [3] Haran K S et al 2017 *Supercond. Sci. Technol.* **30** 123002
- [4] FASTGRID Project 2022 (available at: www.fastgrid-h2020.eu)
- [5] Tixador P et al 2019 *IEEE Trans. Appl. Supercond.* **29** 5603305
- [6] Lacroix C et al 2021 *Supercond. Sci. Technol.* **34** 025015
- [7] Trillaud F, Palanki H, Trociewitz U, Thompson S, Weijers H and Schwartz J 2003 *Cryogenics* **43** 271–9
- [8] Grabovickic R, Lue J, Gouge M, Demko J and Duckworth R 2003 *IEEE Trans. Appl. Supercond.* **13** 1726
- [9] Wang X, Trociewitz U P and Schwartz J 2007 *J. Appl. Phys.* **101** 053904
- [10] Haugen O et al 2007 *IEEE Trans. Appl. Supercond.* **17** 3215–8
- [11] Song H, Davidson M W and Schwartz J 2009 *Supercond. Sci. Technol.* **22** 062001
- [12] van Nugteren J, Dhallé M, Wessel S, Krooshoop E, Nijhuis A and ten Kate H 2015 *Phys. Proc.* **67** 945–51
- [13] Gyuráki R, Sirois F and Grilli F 2018 *Supercond. Sci. Technol.* **31** 034003
- [14] Iannone G, D'Agostino D, Saggese A, Celentano G and Gambardella U 2020 *Cryogenics* **109** 103116
- [15] Marchevsky M 2021 *Instruments* **5** 27
- [16] Akbar A, Yang Z, Wang S, Thévenaz L and Dutoit B 2020 *Supercond. Sci. Technol.* **33** 115003
- [17] Wang X, Trociewitz U P and Schwartz J 2009 *Supercond. Sci. Technol.* **22** 085005
- [18] Giguère J, Lacroix C, Dupuis-Desloges F, Fournier-Lupien J H and Sirois F 2021 *Supercond. Sci. Technol.* **34** 045010
- [19] THEVA Dünnschichttechnik GmbH 2022 (available at: www.theva.com)
- [20] Prusseit W, Hoffmann C, Nemetschek R, Sigl G, Handke J, Lümekemann A and Kinder H 2006 *J. Phys.: Conf. Ser.* **43** 215–8
- [21] Dürrschnabel M, Aabdin Z, Bauer M, Semerad R, Prusseit W and Eibl O 2012 *Supercond. Sci. Technol.* **25** 105007
- [22] Pekarčíková M et al 2020 *Materials* **13** 1832
- [23] Lacroix C and Sirois F 2014 *Supercond. Sci. Technol.* **27** 035003
- [24] Lacroix C, Lapierre Y, Coulombe J and Sirois F 2014 *Supercond. Sci. Technol.* **27** 055013
- [25] Barusco P et al 2022 *ACS Omega* **In Press**
- [26] Lacroix C, Sirois F and Lupien J H F 2017 *Supercond. Sci. Technol.* **30** 064004
- [27] Fournier-Lupien J H, Lacroix C, Hellmann S, Huh J, Pfeiffer K and Sirois F 2018 *Supercond. Sci. Technol.* **31** 125019
- [28] Lacroix C, Fournier-Lupien J H, McMeekin K and Sirois F 2013 *IEEE Trans. Appl. Supercond.* **23** 4701605
- [29] Roy F, Dutoit B, Grilli F and Sirois F 2008 *IEEE Trans. Appl. Supercond.* **18** 29
- [30] Polak M, Barnes P N and Levin G A 2006 *Supercond. Sci. Technol.* **19** 817
- [31] Levin G, Novak K and Barnes P 2010 *Supercond. Sci. Technol.* **23** 014021
- [32] Fournier-Lupien J H, Sirois F and Lacroix C 2021 *Supercond. Sci. Technol.* **34** 085001
- [33] Wilson M N 1987 *Superconducting Magnets* (Oxford: Oxford University Press)
- [34] Dresner L 2002 *Stability of Superconductors* (New York: Kluwer Academic Publishers)
- [35] Iwasa Y 2009 *Case Studies in Superconducting Magnets Design and Operational Issues* 2nd edn (Berlin: Springer)
- [36] Bonura M and Senatore C 2016 *Appl. Phys. Lett.* **108** 242602
- [37] Lacroix C, Lapierre Y, Moret L, Coulombe J and Sirois F 2014 Investigation of the current flow diverter (CFD) concept for increasing the NZPV in 2G HTS CCs *Applied Superconductivity Conf. 2014*